Effect of particle size on the sodium ions utilization efficiency of zeolite-templated carbon as the anode in sodium ion battery

Shuang Tan, Justine Jean, Valerie Pralong, Simona Moldovan, Hailing Guo, Svetlana Mintova

Effect of particle size on the sodium ions utilization efficiency of zeolite-templated carbon as the anode in sodium ion battery

Shuang Tan[a], Justine Jean[b], Valerie Pralong[b], Simona Moldovan[c], Hailing Guo*[a], and Svetlana Mintova*[a][d]

[a] State Key Laboratory of Heavy Oil Processing Key Laboratory of Catalysis, China National Petroleum Corp. (CNPC) China University of Petroleum (East China) Qingdao 266555 (P.R. China) E-mail: guohl@upc.edu.cn, mintova@ensicaen.fr.

[b] Normandie Université, ENSICAEN, UNICAEN, CRISMAT, CNRS, 14000 Caen, France ; Réseau sur le Stockage Electrochimique de l'Énergie (RS2E), 80000 Amiens, France

[c] Institut des Sciences Appliquées de Rouen, Rouen University, Groupe de Physique des Matériaux (GPM), 76801 Rouen, France

[d] Normandie Université, ENSICAEN, UNICAEN, CNRS, Laboratoire Catalyse et Spectrochimie (LCS), 14000 Caen, France

Abstract

A series of zeolite-templated carbon (ZTC) with the particle size of 1μm, 70nm, and 10nm have been prepared. The external surface area and diffusion path of Na^+ inside the ZTC was varied by controlling the size of the zeolite crystals used as templates. The three ZTC samples have been used to store sodium cations (Na^+) for the purpose of sodium-ion batteries (SIB). It was found that the ZTC with a particle size of 10 nm exhibited the highest first discharge capacity of 2116mAh·g^{-1} at a current density of 0.1mA·g^{-1} due to the highest external surface area and more complete filling of the internal pore volume of the ZTC. While the ZTC with 70nm particle size showed better reversible capacity of 180mAh·g^{-1} at a current density of 0.1mA·g^{-1}, and the 10nm size ZTC caused more electrolyte decomposition reaction and more solid electrolyte interphase (SEI) layer on the external surface of the crystals, resulting in a low first coulombic efficiency and poor Na^+ extraction.

Keywords

Zeolite-templated carbon, nanosized zeolite, high sodium storage, carbon anode material

1. Introduction

Due to the abundance of sodium in the earth's crust and the similarity of their energy storage systems to Lithium-ion batteries (LIBs), sodium-ion batteries (SIBs) have drawn a lot of attention as the next-generation energy storage technology[1]. However, owing to the large ionic diameter of Na^+ (1.02Å) compare to Li^+ (0.76Å), the massive volume expansion for accommodating Na^+ has posed serious challenges to the stability of the anode material[2]. Additionally, the electrochemical kinetics of SIBs are also slowed by the large ion diameter of Na^+, which results in poor cycle performance and low capacity. Thus shortening the sodium ion diffusion path to increase its storage rate, along with constructing a stable and sufficient space to accommodate the sodium ion expansion are the main directions for designing high-performance SIB anode materials[3].

Due to their electrical conductivity, chemical stability, accessibility, and sustainability, carbon materials have been exploited as the anode in SIBs. Graphite, the most stable allotrope of carbon, is capable to provide a theoretical capacity of 372 $mAh \cdot g^{-1}$ for lithium ions due to the large layer spacing of 3.35 Å. However, the same space can only provide a theoretical capacity of 35 $mAh \cdot g^{-1}$ for sodium ions[4]. Also, the rate performance is low caused by the larger ionic size and slower kinetics of sodium ions[5]. In order to maximize their Na^+ storage capability and efficiency, researchers have looked into the storage of sodium in carbon materials with various pore configurations to facilitate the accessibility of Na^+ to void structures such as core-shell structure[6], nanosheets[7], microtube[8], nanofiber[9], and porous carbon framework[10, 11]. These examples demonstrate that constructing cavities to accommodate the volume expansion of sodium ions and increasing the external surface area of the material to facilitate the contact of sodium ions with the carbon material is a better way to store Na^+. Recently, the storage behavior of Na^+ in nanoporous attracted considerable interest and it is believed that this could result in hard carbon anodes with prolonged low-potential plateaus and high capacity[12, 13].

Zeolite templated carbon (ZTC) is obtained by calcining carbon-containing precursors in the zeolite channels, the carbon replica of the zeolite channel structure is obtained under high temperature treatment conditions. It has been reported that the abundant and uniform porous of ZTC are crucial for storing small molecules such as CO_2[14], H_2[15], even Li^+[16] and electron[17]. In our previous work[18], the ZTC was used as anode materials of SIB and offered a first discharge capacity of up to 1714 mAh g^{-1} at a current density of 0.1 $A \cdot g^{-1}$. The results suggested that sodium ions can be successfully stored inside the ZTC. Unfortunately, some Na^+ were trapped in the ZTC and unable to be released, leading to a significant capacity loss.

To investigate the storage behavior of Na^+ in ZTC and to further enhance the utilization of Na^+, we reduced the size of the ZTC in order to facilitate the diffusion of Na^+ into the interior space of ZTC. Three ZTC samples with diameters of 1μm, 70 nm, and 10 nm were synthesized and evaluated as SiB anodes at various current densities. The contribution of different place in ZTC to Na^+ storage capacity was evaluated, and the impact of their particle size on the capacity was assessed. The results demonstrated that the nanoporous played a major role in the initial storage of Na^+, and by reducing the particle size of the ZTC, a higher amount of Na^+ was stored but this also caused a significant capacity loss by enhancing the formation of the SEI layer.

Experimental

1.1 Preparation of FAU zeolite crystals with particle size of 1 μm, 70 nm, and 10 nm.

The FAU zeolites with different particle sizes were prepared following the procedure published by Mintova[12]. In a typical synthesis, a clear suspension with the molar ratio of 8 Na_2O: 0.7 Al_2O_3: 10 SiO_2: 160 H_2O (70 nm-FAU) or 9 Na_2O: 0.7 Al_2O_3: 10 SiO_2: 160 H_2O (10 nm-FAU) was aged at ambient conditions for 24 h, and then crystallized at 120 °C for 70 min or 50 °C for 45 h, respectively. The 1 μm FAU zeolite was prepared from a suspension with a molar ratio of 8 Na_2O: 1 Al_2O_3: 10 SiO_2: 400 H_2O; the suspension was aged at ambient conditions for 24h and then subjected to crystallization at 100° C for 12h. The powder obtained after crystallization was labeled as X-FAU (X=1μm, 70nm, and 10nm corresponding to the particle size of FAU zeolite crystals). The crystalline suspensions were filtered to collect the FAU zeolite crystals and then washed with deionized water and dried before use.

1.2 Preparation of FAU-ZTC with particle sizes of 1 μm, 70 nm, and 10 nm.

A vapor impregnation method described elsewhere[18] was used to prepare the FAU-ZTC with various particle sizes. In a typical synthesis, 5 g zeolite (the template) was placed in a vertical glass tube lined with quartz wool, and a stream of furfuryl alcohol (FA) vapor was produced under vacuum and flowed through the zeolite layer. After 1h, the zeolite template was saturated with the FA, and then the atmospheric pressure was restored and the zeolite was left to continue absorbing FA at ambient temperature for 24 hours. The zeolite samples loaded with FA were then washed with mesitylene to remove the excess of FA adsorbed on the external surface. The excess mesitylene was then removed by heating at 80°C for 12 hours. Then the FA-loaded FAU zeolite samples were heated at 150°C for 8 hours in nitrogen to pre-polymerize the FA. The pre-polymerized samples were then heated at 900°C for 4h with a heating rate of 5°C/min under a nitrogen atmosphere. Finally, the zeolite template was removed from the ZTC products by acid etching with a solution of 0.4M HF/0.2M HCl. Finally, the ZTC samples were washed with distilled water and dried at 100°C overnight. The obtained samples were labeled as X-FAU-ZTC (X=1μm, 70nm, or 10nm).

2. Characterization

The morphology and crystal size of the samples were characterized using a JEOL SEM-7900F scanning electron microscope (SEM) with an acceleration voltage of 5 kV. The Scanning Transmission Electron Microscopy (STEM) experiments were performed on a double corrected Analytical JEOL ARM200CF TEM operated at 200kV for imaging and 120kV for mapping. The TEM is equipped with a 100mm^2 Centurio Energy Dispersive X Rays (EDX) detector for the chemical analysis of the constituents. The samples were prepared under ultrasound treatment of powders in ethanol obtained by mechanical scratching of the cathode materials after the different treatments. The solution was drop cast on a holey Carbon membrane deposited on a 300 mesh Au grid adapted for the TEM experiments. Elemental maps (256 x 256px) were acquired using the Analysis Station (Jeol) software with a scanning speed of 0.02 ms/px in order to minimize the damaging effect of the electron beam and a spatial tracking algorithm was applied every 60 seconds. The same software was employed for the qualitative and quantitative analysis of the experimental data. X-ray powder diffraction (XRD) patterns were collected using a Bruker D8 Advance. The N_2 adsorption-desorption experiments were performed at 77 K using a

Quantachrome Autosorb iQ3 gas-sorption analyzer. The micropore volume was calculated from the *v-t* plot. The pore size distribution was determined using the Quenched solid density functional theory (QSDFT) method.

2.1 Electrochemical test

The electrochemical performance of the ZTC samples was evaluated using half-cells assembled in a glove box. The powder samples were mixed with super P and poly vinylidene fluoride in a weight ratio of 8:1:1 in N-methyl-2-pyrrolidinone to form a homogeneous slurry, which were then deposited on a Cu foil and dried in a vacuum oven at 80°C for 12 h. Sodium metal foils were used as counter and reference electrodes. A solution of 1 mol·L^{-1} $NaClO_4$ in ethylene carbonate/diethyl carbonate (1/1; v/v) with 5 wt.% fluoroethylene carbonate was used as the electrolyte and Celgard 2400 was used as the separator. The active materials mass loaded on each round of Cu foil was about 0.7 mg·cm^{-2}. Cyclic voltammetric measurements with a scan rate of 0.1 mV·s^{-1} were performed on a CHI760D electrochemical workstation. Galvanostatic charge/discharge measurements were performed using a multichannel battery testing system (LAND CT2001A) in a voltage range of 0.01–3 V for anodes versus Na/Na^+ at different constant current densities.

The amount of Na^+ accommodated in supercages of the ZTC was calculated using the following equations:

$$N = \frac{\frac{C*3.6*N_a}{F}}{\frac{V_{micro}}{V_{pore}}} \quad (1)$$

$$V_{pore} = \frac{4}{3}\pi(\frac{R}{2})^3 \quad (2)$$

where C is Capacity, F is Faraday constant, N_a is Avogadro's constant, V_{micro} is Micropores volume of ZTC, V_{pore} is single supercage volume of ZTC, and R is pore diameter of ZTC.

3. Results and Discussion

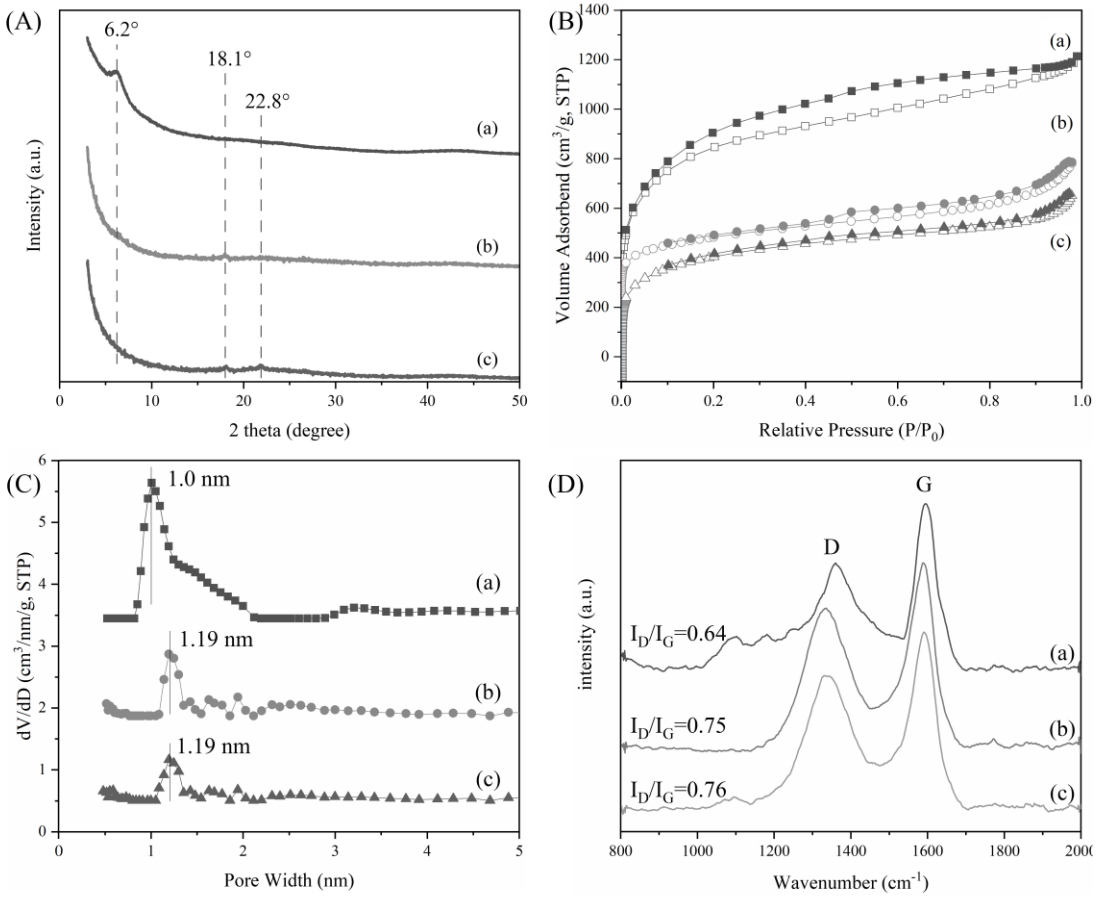

Figure 1 XRD patterns (A), N_2 adsorption-desorption isotherms (B), pore size distribution (C), and RAMAN spectra (D) of samples 1μm-FAU-ZTC (a), 70nm-FAU-ZTC (b), and 10nm-FAU-ZTC (c).

The structure of FAU-type zeolite (Figure S1A), and ZTC (Figure 1A) were determined by X-ray diffraction. All three samples of zeolites with various particle sizes exhibit characteristic Bragg peaks corresponding to the FAU-framework structure. As the particle size decreases, the intensity of the peaks decreased and the half-height width of the peak expands, indicating that the structure is less ordered. The non-negligible decrease in crystallinity led to a decrease in the specific surface area and micropore volume of the zeolite templates as confirmed by nitrogen physisorption analysis (Figure S2A, Table S1). In comparison to sample 1μm-FAU, the specific surface areas of 70nm-FAU and 10 nm-FAU decreased by 26% and 50%, respectively. Similar to other ZTC materials synthesized with furfuryl alcohol[19], the sample 1μm-FAU-ZTC exhibits a weak peak at 6.3° 2θ in the XRD pattern, which is a replica of 111 crystal plane of the FAU zeolite[20, 21]. This indicates that the 1μm-FAU-ZTC sample has faithfully replicated the FAU zeolite structure. Only weak peaks or no peaks at the same position in the XRD patterns of samples 70 nm-FAU-ZTC and 10 nm-FAU-ZTC were observed as a consequence of the small particle size and partial collapse of nanosized zeolite template at high temperature[22]. At the same time, no broad peaks representing the disordered graphitic structure of the amorphous carbon were observed at 25° 2θ for all three samples[23], suggesting that the ZTC samples have formed a self-standing porous carbon skeleton by replicating the zeolite framework rather than amorphous stacked carbon.

As shown in Figure 1B, all three ZTC samples exhibited a type I isotherm[24] which is composed of micropores, proving that the parent zeolite's microporous structure has been successfully replicated (Figure 1B). The adsorption-desorption isotherm of sample 1μm-FAU-ZTC contains a "low-pressure hysteresis". This phenomenon has been reported for various ZTC materials[25-27], which has been attributed to carbon particles swelling during the nitrogen adsorption measurements, or to the strong interactions of nitrogen molecules with the carbon surface[28, 29]. The isotherms of samples 70nm-FAU-ZTC and 10nm-FAU-ZTC differ slightly from that of sample 1μm-FAU-ZTC. An upward turn with a weak hysteresis at high relative pressure was recorded. This hysteresis loop indicates the mesoporosity generated from interparticle space due to the packing of well-defined individual particles with similar sizes[22]. The external surface area of the ZTC increases as the crystal size decreases, but the total surface area and the microporous surface area (S_{mic}) decrease substantially (Table 1). Apparently, the decrease of S_{mic} of the parent FAU zeolite template leads to the decrease of S_{mic} in the carbon replica.

Table 1 N_2 adsorption analysis data of ZTC samples.

Sample	S_{BET} ($m^2 \cdot g^{-1}$)[a]	S_{mi} ($m^2 \cdot g^{-1}$)[b]	S_{ex}($m^2 \cdot g^{-1}$)	V_t ($cm^3 \cdot g^{-1}$)[c]	V_{mi} ($cm^3 \cdot g^{-1}$)[d]
1μm-FAU-ZTC	2373	1937	245	1.87	1.06
70nm-FAU-ZTC	2154	1864	290	1.31	0.89
10nm-FAU-ZTC	1612	1270	342	1.14	0.68

[a] BET specific surface area was calculated from the adsorption branch in P/P_0 = 0.02-0.15.

[b] Micropore surface was calculated by the t-plot method.

[c] Total pore volume was determined at P/P_0 = 0.97.

[d] Micropore volume was calculated from the t-plot method.

Figure 1D shows the RAMAN spectra of the carbon samples, which exhibit D and G peaks at 1380cm^{-1} and 1600cm^{-1} corresponding to the A_{1g} ring respiration mode and the E_{2g} vibration between adjacent sp^2 hybridized carbon atoms, respectively[30]. The integrity of the carbon structure network, or the level of graphitization, is indicated by the intensity ratio of D and G peaks. The I_D/I_G ratio of 1μm-FAU-ZTC, 70nm-FAU-ZTC, and 10nm-FAU-ZTC is 0.64, 0.75, and 0.76, respectively. The 1μm-FAU-ZTC has lower I_D/I_G ratio as the template contains larger zeolite particles that are more robust at high temperature and can provide a stable environment for the growth of the carbon skeleton[31, 32]. In contrast, samples 70nm-FAU-ZTC and 10nm-FAU-ZTC have higher I_D/I_G ratio due to the possible collapse of the small zeolite particles at high temperature and presence of defects in the carbon lattice.

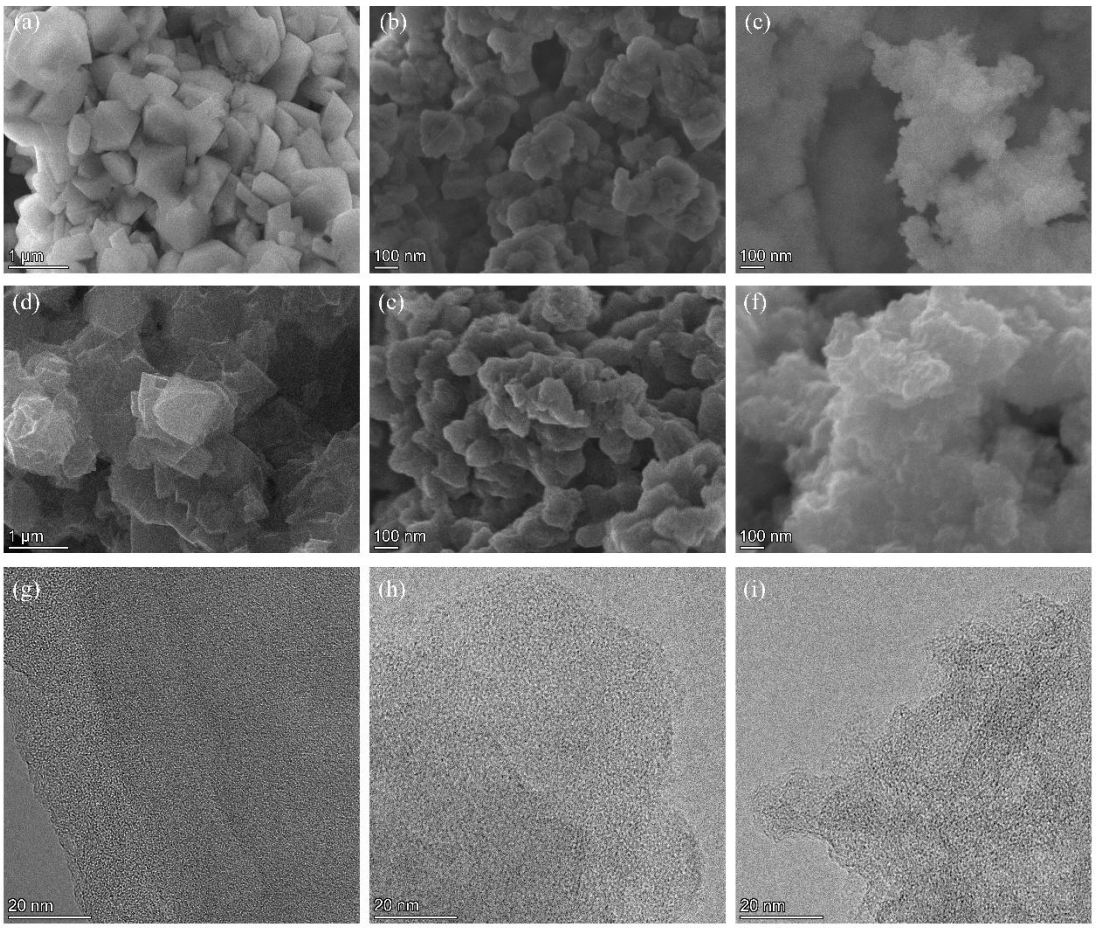

Figure 2 SEM pictures of samples 1µm-FAU (a), 70nm-FAU (b), 10nm-FAU (c); SEM and TEM pictures of samples 1µm-FAU-ZTC (d, g), 70nm-FAU-ZTC (e, h), and 10nm-FAU-ZTC (f, i).

SEM images of the ZTC samples reveal the progressive decrease in the particle size of the zeolite template and the ZTCs (Figure 2). Both 1µm-FAU and 1µm-FAU-ZTC samples exhibit the classical ortho-octahedral shape, which suggests that the carbon replicates the zeolite morphology closely. The intergrowth in sample 1µm-FAU is possible causing the interconnections in the carbon replica. The 70nm-FAU sample contains individual crystals with a size of 70-150 nm, and less sharp edges along with a change in crystal structure from ortho-octahedral to ellipsoidal. This phenomenon is also observed for sample 70 nm-FAU-ZTC due to the exact replication of the crystal structure of the template. The crystals diameter of sample 10nm-FAU is in the range of 10-40 nm, and these crystals transformed into nearly spherical blocks. Due to the high surface energy and the capillary effect of water during the drying, the small size carbon replicas are easily agglomerated[12]. Therefore no individual particles have been seen for samples 70nm-FAU-ZTC and 10nm-FAU-ZTC by TEM. All three samples exhibited homogeneous microporous structure thus demonstrating the successful replication of the FAU micropores [33, 34].

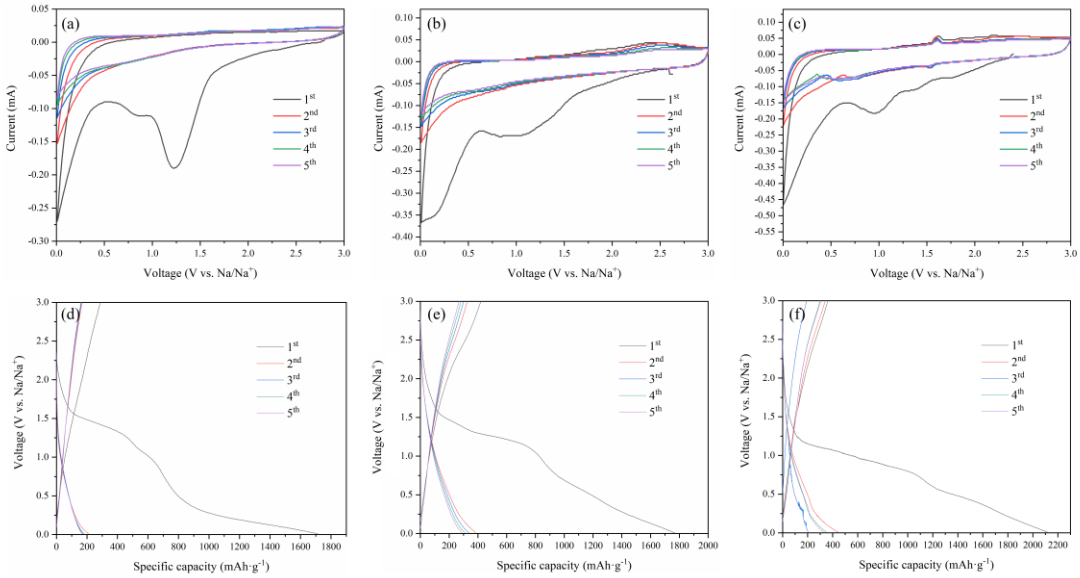

Figure 3 Cyclic voltammograms (CV) at a scan rate of 0.1 mV·s $^{-1}$ and galvanostatic charge-discharge profiles (GCD) tested at a current density of 0.1 A·g^{-1} for samples 1μm-FAU-ZTC (a, d), 70nm-FAU-ZTC (b, e), and 10nm-FAU-ZTC (c, f) at five cycles

The sodiation and de-sodiation behavior of the ZTCs electrode during the first five charges and discharges were tested by cyclic voltammograms (CV) (Figure 3a, b, and c). Three peaks located at 0.01 V, 0.86 V, and 1.22 V can be seen in the first negative scan of sample 1μm-FAU-ZTC. The peak at 0.01 V represents the porefilling of Na^+ and the adsorption of Na^+ on defects and edges of ZTC[35, 36]. The two peaks located at 0.86 V and 1.22 V that disappeared in the subsequent cycles are due to the irreversible reaction between Na^+ and surface functional groups[7], decomposition of electroyte[37], and formation of SEI layers[38]. The second CV scan did not show any peaks except the one at 0.01 V, indicating that a stable SEI layer was formed and the sodium ion storage behavior of porefilling and the adsorption on the edges and defects sites is predominant [39, 40]. The first CV curves for the three samples are compared (Figure S3), the observed peaks were found to become larger with decreasing the particle size of the zeolite template crystals, resulting in enhanced sodium storage. The peaks of surface reaction and SEI layer formation are also enhanced due to the higher external surface area of the template[41]. For the same reason, the de-sodiation current at 3.0-1.0 V strengthens, indicating that the sodium ions adsorbed on the external surface of ZTCs are being released. In contrast to the other two samples, the subsequent CV curves for sample 10nm-FAU-ZTC revealed a pair of redox peaks at 1.53 V and 1.59 V. Peaks at similar positions have been reported earlier; the formation of pseudometals in the micropores of carbon materials was suggested[42, 43]. This emphasizes the adequacy of sodium ions to enter the pores of sample 10nm-FAU-ZTC. The first five galvanostatic charge-discharge (GCD) profiles of samples 1μm-FAU-ZTC, 70nm-FAU-ZTC, and 10nm-FAU-ZTC at 100 mA·g^{-1} are shown in Figures 3d, e, and f, respectively. All three samples show a voltage profile of a sloping line without distinct plateaus. The curves all start with a descending slope with a continuous curvature in the high-voltage region, which is the consequence of the quick adsorption of Na^+ to the defect or edge sites of ZTC[44, 45]. Unlike the micropore filling that has been reported in hard carbon materials, the filling of the supercages of ZTC does not show a long and distinct plateau, but

rather a steady decreasing slope at 1.5-0.1V, which is similar to carbon nanotubes and activated carbon with small interspaces used to store sodium ions[7, 9, 42, 46, 47].

The first discharge capacity and first charge capacity of the three ZTC anodes are presented in Table 2. It can be seen that the smaller particle sizes of samples 70nm-FAU-ZTC and 10nm-FAU-ZTC resulted in a better performance compare to sample 1μm-FAU-ZTC. Among all samples, the 10nm-FAU-ZTC with the smallest particle size exhibited the highest first discharge capacity of 2116 $mAh \cdot g^{-1}$ due to the highest internal space accessibility. The first discharge capacity contributed by surface reaction and SEI layer formation was calculated using the shoulder region around 1.5V. For samples 1μm-FAU-ZTC, 70nm-FAU-ZTC, and 10nm-FAU-ZTC, the contribution of surface reaction and SEI layer formation has been calculated to be 350, 550, and 850 $mAh \cdot g^{-1}$, respectively (calculation details presented in Figure S4). After excluding the capacity contributed by the external adsorbed Na^+ and SEI formation, the first discharge capacity of samples 1 μm-FAU-ZTC, 70nm-FAU-ZTC, and 10nm-FAU-ZTC is equal to 13.7, 22.6, and 31.0 Na^+ stored in each supercage, respectively. It can be seen that the short diffusion path of the small particles greatly facilitates the Na^+ to enter the supercage of ZTC. However, the first charge capacity exhibited a significant loss, indicating that only 1.5, 4.9, and 4.6 Na^+ were able to be re-extracted from the supercages of 1μm-FAU-ZTC, 70nm-FAU-ZTC, and 10nm-FAU-ZTC, respectively. The amount of Na^+ that can be re-extracted from the supercages of 10 nm-FAU-ZTC is lower than that of 70 nm-FAU-ZTC, which is the result of more SEI layer caused by the large external surface area. Thus 70nm-FAU-ZTC has shown the highest first Coulomb efficiency (23.8%). The shoulder representing the formation of SEI disappears in the subsequent GCD curves for all three samples, implying that a stable SEI layer has been formed during the first discharge. In addition to this, the Na^+ adsorbed on the external surface contributed mostly to the capacity in the subsequent cycles, for the discharge curve is composed mostly by straight lines with a consistent slope[48]. However, the contribution of the supercage to the capacity still tends to increase with the increase of the external surface area of the ZTC, which indicates that only the Na^+ stored in the supercages close to the external surface can be reversibly adsorbed and desorbed.

Table 2 The initial discharge capacity, initial charge capacity, and stable reversible capacity of ZTC samples at $0.1A \cdot g^{-1}$.

Sample	First discharge capacity ($mAh \cdot g^{-1}$)	First charge capacity ($mAh \cdot g^{-1}$)	First Coulumbic efficiency (%)	Stable reversible capacity ($mAh \cdot g^{-1}$)[a]	Reference
1μm-FAU-ZTC	1718	288	16.8	120	This work
70nm-FAU-ZTC	1767	420	23.8	180	This work
10nm-FAU-ZTC	2116	360	17.0	170	This work
Activated carbon	~820	~150	~18	~100	[39]
Graphene oxide nanosheet	~240	~210	~87	~150	[40]
Carbon nanotubes	~80	~70	~87	~60	[43]

[a] stable reversible capacity is sampled after 50 cycles at 100 mA·cm^{-2}.

The performance of the three samples after the first 100 cycles was also evaluated and the results are summarized in Figure 4. After several cycles, the ZTC still displays an appreciable reversible capacity and a very high coulombic efficiency. The performance of the samples remained stable even after hundreds of cycles (Figure S5), demonstrating the stability of the ZTC structure. For comparison, the performance of other carbon materials reported earlier are also summarized in Table 2. Commercial activated carbon has a high surface area and complex pore structure, but as a typical anode carbon material, its performance is much lower than that of ZTC. Graphene oxide nanosheets and carbon nanotubes have a polycarbon ring structure similar to that of ZTC, but they do not show significant capacity. However, the first coulumbic efficiency of ZTC samples is still lower than the carbon materials presented in Table 2, which is a main difficult for the ZTC to be considered for practical application.

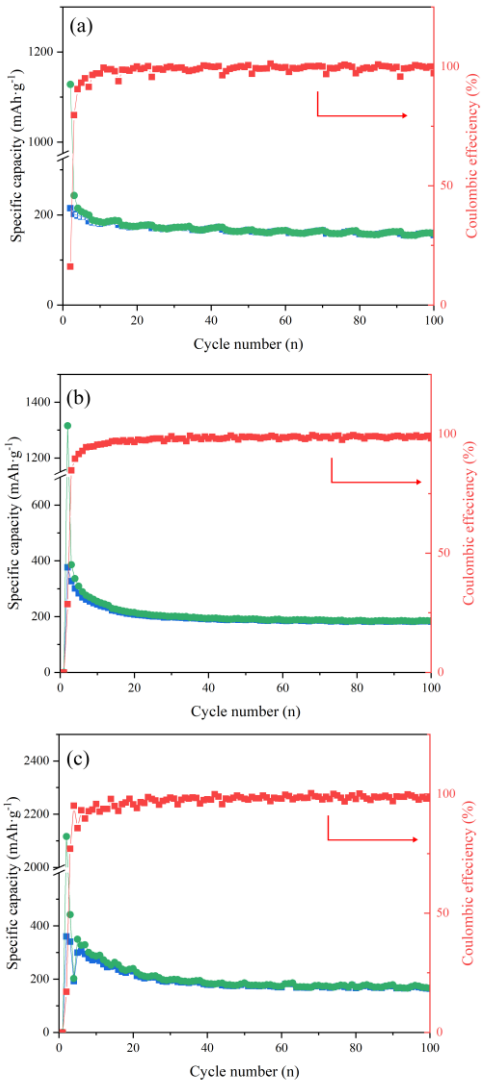

Figure 4 The cycle performance of samples 1μm-FAU-ZTC (a), 70nm-FAU-ZTC (b), and 10nm-FAU-ZTC (c) at 100mA·g^{-1}

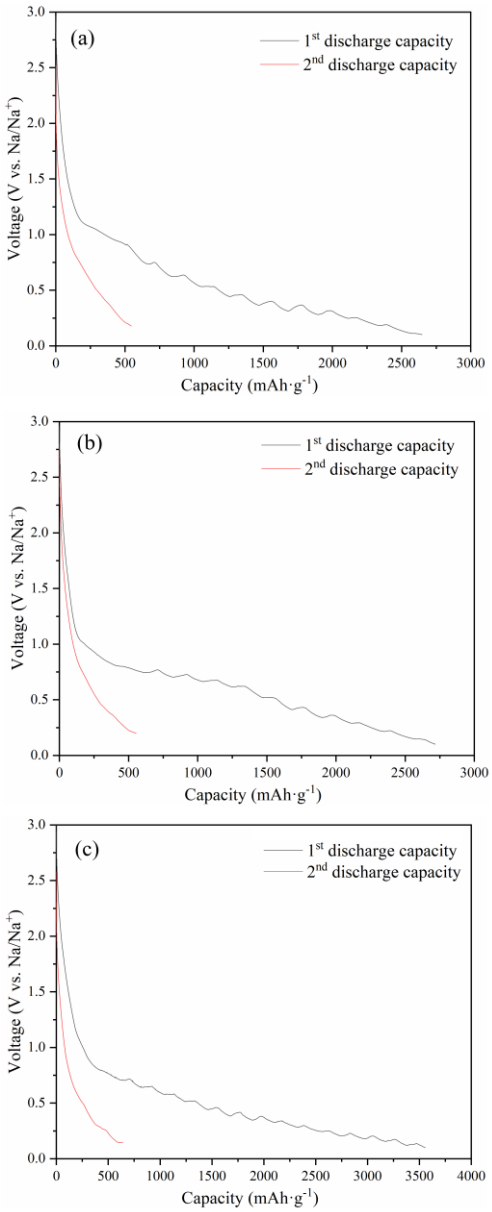

Figure 5 First and second galvanostatic discharge profiles of samples 1μm-FAU-ZTC (a), 70nm-FAU-ZTC (b), and 10nm-FAU-ZTC (c) at 9mA·g^{-1}

In order to fully explore the sodium storage capacity of ZTC materials and verify the sodium storage mechanism, the samples were discharged with a very low current density (9mA·g^{-1}) resulting in more mild surface reaction, SEI layer formation, and more complete porefilling. Thus the sodium storage potential of the internal pores of ZTC can be fully exploited. The first and second discharge capacities of the samples are present in Figure 5. Because of the milder surface reaction and SEI formation, there is no obvious plateau around 1.5 V in the first discharge curve to calculate the resulting capacity contribution. However, it can still be seen that at low current densities, 10nm-FAU-ZTC exhibits the highest first discharge capacity of 3555mAh·g^{-1}, even though it includes the contribution of more SEI layer formed due to higher external surface area. After the first charge and discharge, the contribution of the SEI layer was excluded, and the second discharge capacity of sample 10nm-FAU-ZTC (642mAh·g^{-1}) showed that still 8.07 sodium

ions could enter and be stored in each supercage during the second cycle. The sodium ions stored in samples 1μm-FAU-ZTC and 10 nm-FAU-ZTC are 4.18 and 6.45, respectively. It can be seen that the utilization efficiency of the supercages increases with decreasing the particle size at low concentration difference polarization due to the very low current density. This confirms that the amount of the SEI layer is an important factor affecting the ZTC capacity at 100mA·g^{-1} [45, 49-52].

Based on the presented results, the filling process of ZTC by sodium ions is illustrated schematically in Figure 6. First, the sodium ions adsorbed on the external surface of the ZTC[46, 51, 52]. Second, the sodium ions start to form an SEI layer and enter the ZTC's supercages and adsorb on the inner surface. Finally, the Na^+ continues to migrate to the inner part of the ZTC until saturated[35, 53]. During the sodium removal process, only sodium ions adsorbed on the external layer of the ZTC and in the supercages near the external surface can desorb, while the sodium ions adsorbed in the internal voids of ZTC are retained and cannot leave due to the high adsorption energy and long diffusion path. When the sodiation process occurs on ZTC crystals with large particle size, the pores are unable to be fully filled due to the extended diffusion path. In contrast, the short diffusion path of the small ZTC particles can take full advantage of the supercage, and more sodium ions can be filled into the supercage and stored in a desolvated form, but at the same time, the high external surface area is also responsible for the formation of more SEI layers and this hinders the sodium ions from being extracted from the supercage at high current densities.

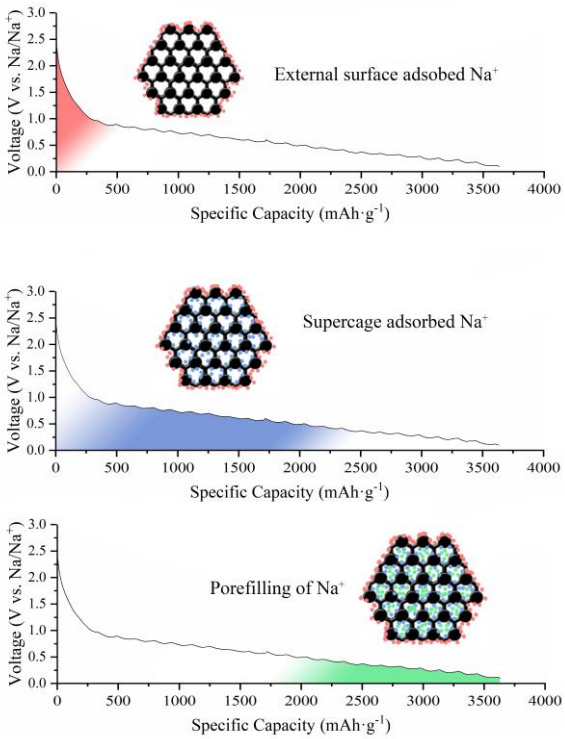

Figure 6 Schematic diagram of ZTC with different particle sizes storing sodium ions on the external surface, internal surface of supercages and porefilling

4. Conclusions

In summary, ZTC with crystal dimensions of 1 μm, 70 nm, and 10 nm were synthesized. It was shown that the size of the ZTC particles has a significant effect on their performance as an anode for sodium batteries. On the one hand, increasing the crystal size of the ZTC was beneficial to reduce the contact area with the electrolyte, which suppressed the side reactions and the SEI layer generation occurring on the external surface, resulting in a better first Coulomb efficiency. On the other hand, the large size of the crystals increased the diffusion path of sodium ions, and the pores of ZTC cannot be fully utilized, causing the decrease of both the first discharge capacity and reversible capacity. Therefore, sample 70nm-FAU-ZTC with intermediate particle size was found to exhibit the highest first coulombic efficiency (23.8%) and reversible capacity (180mAh·g^{-1} at a current density of 100mA·g^{-1}), while sample 10nm-FAU-ZTC showed the highest first discharge capacity (2116mAh·g^{-1} at a current density of 100mA·g^{-1}). The potential of ZTC materials to store sodium ions was fully explored at very low current densities (9mA·g^{-1}): sample 10nm-FAU-ZTC exhibited the highest first discharge capacity (3555mAh·g^{-1}) and second discharge capacity (642mAh·g^{-1}). The results suggested that the ZTC materials can still be further optimized to improve their performance as a SIB anode material.

ACKNOWLEDGMENT

The authors gratefully acknowledged funding from the National Key Research and Development Program of China of Ministry of Science and Technology (2022YFE116000), the National Natural Science Foundation of China [Grant No. 22175200, No. 21975285], and Innovation Fund of Science and Technology Project of Fujian Province (2022C0021). Thanks to the Yanpeng Li from Advanced Chemical Engineering and Energy Materials Researcher Center in China University of Petroleum for the STEM characterization.

REFERENCES

1. Delmas, C., Sodium and Sodium-Ion Batteries: 50 Years of Research. *Adv. Energy Mater.* **2018,** *8* (17).

2. Hwang, J. Y.; Myung, S. T.; Sun, Y. K., Sodium-ion batteries: present and future. *Chem Soc Rev* **2017,** *46* (12), 3529-3614.

3. Slater, M. D.; Kim, D.; Lee, E.; Johnson, C. S., Sodium-Ion Batteries. *Adv. Funct. Mater.* **2013,** *23* (8), 947-958.

4. Wen, Y.; He, K.; Zhu, Y.; Han, F.; Xu, Y.; Matsuda, I.; Ishii, Y.; Cumings, J.; Wang, C., Expanded graphite as superior anode for sodium-ion batteries. *Nature Communications* **2014,** *5* (1), 4033.

5. Wang, L.; He, X.; Li, J.; Sun, W.; Gao, J.; Guo, J.; Jiang, C., Nano-Structured Phosphorus Composite as High-Capacity Anode Materials for Lithium Batteries. *Angew Chem Int Ed Engl* **2012,**

51 (36), 9034-9037.

6. Sun, B.; Zhang, Q.; Zhang, C.; Xu, W.; Wang, J.; Yuan, G.; Lv, W.; Li, X.; Yang, N., A Passionfruit- Like Carbon- Confined Cu2ZnSnS4 Anode for Ultralong- Life Sodium Storage. *Adv. Energy Mater.* **2021**.

7. Xia, J. L.; Yan, D.; Guo, L. P.; Dong, X. L.; Li, W. C.; Lu, A. H., Hard Carbon Nanosheets with Uniform Ultramicropores and Accessible Functional Groups Showing High Realistic Capacity and Superior Rate Performance for Sodium-Ion Storage. *Adv. Mater.* **2020,** *32* (21), 2000447.

8. Li, Y.; Hu, Y.-S.; Titirici, M.-M.; Chen, L.; Huang, X., Hard Carbon Microtubes Made from Renewable Cotton as High-Performance Anode Material for Sodium-Ion Batteries. *Adv. Energy Mater.* **2016,** *6* (18), 1600659.

9. Ren, Q.; Shi, Z.; Yan, L.; Zhang, F.; Fan, L.; Zhang, L.; Lv, W., High-performance sodium-ion storage: multi-channel carbon nanofiber freestanding anode contrived via ingenious solvent-induced phase separation. *J. Mater. Chem. A* **2020,** *8* (38), 19898-19907.

10. Hou, H.; Banks, C. E.; Jing, M.; Zhang, Y.; Ji, X., Carbon Quantum Dots and Their Derivative 3D Porous Carbon Frameworks for Sodium-Ion Batteries with Ultralong Cycle Life. *Adv. Mater.* **2015,** *27* (47), 7861-7866.

11. Wang, Y.; Wang, C.; Guo, H.; Wang, Y.; Huang, Z., A nitrogen-doped three-dimensional carbon framework for high performance sodium ion batteries. *RSC Advances* **2017,** *7* (3), 1588-1592.

12. Li, Y.; Lu, Y.; Meng, Q.; Jensen, A. C. S.; Zhang, Q.; Zhang, Q.; Tong, Y.; Qi, Y.; Gu, L.; Titirici, M. M.; Hu, Y. S., Regulating Pore Structure of Hierarchical Porous Waste Cork- Derived Hard Carbon Anode for Enhanced Na Storage Performance. *Adv. Energy Mater.* **2019,** *9* (48).

13. Matei Ghimbeu, C.; Górka, J.; Simone, V.; Simonin, L.; Martinet, S.; Vix-Guterl, C., Insights on the Na+ ion storage mechanism in hard carbon: Discrimination between the porosity, surface functional groups and defects. *Nano Energy* **2018,** *44*, 327-335.

14. Youn, H.-K.; Kim, J.; Chandrasekar, G.; Jin, H.; Ahn, W.-S., High pressure carbon dioxide adsorption on nanoporous carbons prepared by Zeolite Y templating. *Mater. Lett.* **2011,** *65* (12), 1772-1774.

15. Musyoka, N. M.; Rambau, K. M.; Manyala, N.; Ren, J.; Langmi, H. W.; Mathe, M. K., Utilization of waste tyres pyrolysis oil vapour in the synthesis of Zeolite Templated Carbons (ZTCs) for hydrogen storage application. *J Environ Sci Health A Tox Hazard Subst Environ Eng* **2018,** *53* (11), 1022-1028.

16. Kwon, Y.; Kim, K.; Park, H.; Shin, J. W.; Ryoo, R., Anomalously High Lithium Storage in Three-Dimensional Graphene-like Ordered Microporous Carbon Electrodes. *J. Phys. Chem. Lett. C* **2018,** *122* (9), 4955-4962.

17. Mostazo-López, M. J.; Ruiz-Rosas, R.; Castro-Muñiz, A.; Nishihara, H.; Kyotani, T.; Morallón, E.; Cazorla-Amorós, D., Ultraporous nitrogen-doped zeolite-templated carbon for high power density aqueous-based supercapacitors. *Carbon* **2018,** *129*, 510-519.

18. Tan, S.; Wang, C. X.; Foucaud, Y.; Badawi, M.; Guo, H. L.; Sun, K.; Yang, G.; Mintova, S., Ordered sodium zeolite-templated carbon with high first discharge capacity for sodium battery application. *Micropor. Mesopor. Mat.* **2022,** *336*, 111853.

19. Zhang, H.; Liu, Q.; Fang, Y.; Teng, C.; Liu, X.; Fang, P.; Tong, Y.; Lu, X., Boosting Zn-Ion Energy Storage Capability of Hierarchically Porous Carbon by Promoting Chemical Adsorption. *Adv. Mater.* **2019,** *31* (44), e1904948.

20. Antoniou, M. K.; Diamanti, E. K.; Enotiadis, A.; Policicchio, A.; Dimos, K.; Ciuchi, F.; Maccallini, E.; Gournis, D.; Agostino, R. G., Methane storage in zeolite-like carbon materials.

Micropor. Mesopor. Mat. **2014,** *188*, 16-22.
21. Kwon, Y.; Kim, K.; Ryoo, R., N-doped zeolite-templated carbon as a metal-free electrocatalyst for oxygen reduction. *RSC Advances* **2016,** *6* (49), 43091-43097.
22. Parmentier, J.; Valtchev, V.; Gaslain, F.; Tosheva, L.; Ducrot-Boisgontier, C.; Möller, J.; Patarin, J.; Vix-Guterl, C., Effect of the zeolite crystal size on the structure and properties of carbon replicas made by a nanocasting process. *Carbon* **2009,** *47* (4), 1066-1073.
23. Shi, J.; Li, W.; Li, D., Rapidly reversible adsorption of methane with a high storage capacity on the zeolite templated carbons with glucose as carbon precursors. *Colloids and Surfaces A: Physicochemical and Engineering Aspects* **2015,** *485*, 11-17.
24. Armandi, M.; Bonelli, B.; Cho, K.; Ryoo, R.; Garrone, E., Study of hydrogen physisorption on nanoporous carbon materials of different origin. *International Journal of Hydrogen Energy* **2011,** *36* (13), 7937-7943.
25. Choi, S.; Kim, H.; Lee, S.; Wang, Y.; Ercan, C.; Othman, R.; Choi, M., Large-scale synthesis of high-quality zeolite-templated carbons without depositing external carbon layers. *Chem. Eng. J.* **2015,** *280*, 597-605.
26. Lu, H.; Kim, K.; Kwon, Y.; Sun, X.; Ryoo, R.; Zhao, X. S., Zeolite-templated nanoporous carbon for high-performance supercapacitors. *J. Mater. Chem. A* **2018,** *6* (22), 10388-10394.
27. Liu, Y.; Wang, T.; Wang, J.; Pan, W.-P., Enhancing inward and outward mass transport during chemical vapor deposition of pyrolytic carbon for better synthesis of ZTC. *Micropor. Mesopor. Mat.* **2022,** *334*.
28. Su, F.; Zhao, X. S.; Lv, L.; Zhou, Z., Synthesis and characterization of microporous carbons templated by ammonium-form zeolite Y. *Carbon* **2004,** *42* (14), 2821-2831.
29. Ma, Z.; Kyotani, T.; Tomita, A., Synthesis methods for preparing microporous carbons with a structural regularity of zeolite Y. *Carbon* **2002,** *40* (13), 2367-2374.
30. Zhao, W.; Basnet, B.; Kim, I. J., Carbon nanotube formation using zeolite template and applications. *Journal of Advanced Ceramics* **2012,** *1* (3), 179-193.
31. Nishihara, H.; Yang, Q.-H.; Hou, P.-X.; Unno, M.; Yamauchi, S.; Saito, R.; Paredes, J. I.; Martínez-Alonso, A.; Tascón, J. M. D.; Sato, Y.; Terauchi, M.; Kyotani, T., A possible buckybowl-like structure of zeolite templated carbon. *Carbon* **2009,** *47* (5), 1220-1230.
32. Cui, X.; Xu, Y.; Chen, L.; Zhao, M.; Yang, S.; Wang, Y., Ultrafine Pd nanoparticles supported on zeolite-templated mesocellular graphene network via framework aluminum mediation: An advanced oxygen reduction electrocatalyst. *Applied Catalysis B: Environmental* **2019,** *244*, 957-964.
33. Itoi, H.; Kasai, Y.; Morishita, K.; Suzuki, R.; Gotoh, Y.; Matsuoka, C.; Miyaji, M.; Hirade, R.; Tanabe, Y.; Iwata, H.; Ohzawa, Y., Facile synthesis of high surface area zeolite-templated carbons using divinylbenzene and propylene as carbon sources. *Micropor. Mesopor. Mat.* **2021,** *326*.
34. Wang, J.; Wang, T.; Wang, Q.; Pan, W.-P., Removing ionic and organic mercury from light hydrocarbon liquids by ordered zeolite-templated carbon doped with sulphur. *Journal of Cleaner Production* **2022,** *339*.
35. Morikawa, Y.; Nishimura, S. i.; Hashimoto, R. i.; Ohnuma, M.; Yamada, A., Mechanism of Sodium Storage in Hard Carbon: An X- Ray Scattering Analysis. *Adv. Energy Mater.* **2019,** *10* (3), 1903176.
36. Li, Q.; Zhu, Y.; Zhao, P.; Yuan, C.; Chen, M.; Wang, C., Commercial activated carbon as a novel precursor of the amorphous carbon for high-performance sodium-ion batteries anode. *Carbon* **2018,** *129*, 85-94.

37. Mahmood, A.; Li, S.; Ali, Z.; Tabassum, H.; Zhu, B.; Liang, Z.; Meng, W.; Aftab, W.; Guo, W.; Zhang, H.; Yousaf, M.; Gao, S.; Zou, R.; Zhao, Y., Ultrafast Sodium/Potassium-Ion Intercalation into Hierarchically Porous Thin Carbon Shells. *Adv. Mater.* **2019,** *31* (2), e1805430.

38. Yu, Q.; Dong, T.; Qiu, R.; Wang, H., Sulfur and nitrogen dual-doped carbon nanofiber with enlarged interlayer distance as a superior anode material for sodium-ion capacitors. *Materials Research Bulletin* **2021,** *138*.

39. Zhao, X.; Wang, H.-E.; Chen, X.; Cao, J.; Zhao, Y.; Garbe Neale, Z.; Cai, W.; Sui, J.; Cao, G., Tubular MoO2 organized by 2D assemblies for fast and durable alkali-ion storage. *Energy Storage Materials* **2018,** *11*, 161-169.

40. Bobyleva, Z. V.; Drozhzhin, O. A.; Dosaev, K. A.; Kamiyama, A.; Ryazantsev, S. V.; Komaba, S.; Antipov, E. V., Unveiling pseudocapacitive behavior of hard carbon anode materials for sodium-ion batteries. *Electrochim. Acta* **2020,** *354*.

41. Zhang, Z.; Wang, R.; Zeng, J.; Shi, K.; Zhu, C.; Yan, X., Size Effects in Sodium Ion Batteries. *Adv. Funct. Mater.* **2021,** *31* (52).

42. Morita, R.; Gotoh, K.; Fukunishi, M.; Kubota, K.; Komaba, S.; Nishimura, N.; Yumura, T.; Deguchi, K.; Ohki, S.; Shimizu, T.; Ishida, H., Combination of solid state NMR and DFT calculation to elucidate the state of sodium in hard carbon electrodes. *J. Mater. Chem. A* **2016,** *4* (34), 13183-13193.

43. Yang, S.; Wang, S.; Chen, D.; He, W.; Li, L., Boosting sodium storage performance of Mo2C via nitrogen-doped carbon sphere encapsulation and rGO wrapping. *Chem. Eng. J.* **2021,** *413*, 127471.

44. Chen, D.; Zhang, W.; Luo, K.; Song, Y.; Zhong, Y.; Liu, Y.; Wang, G.; Zhong, B.; Wu, Z.; Guo, X., Hard carbon for sodium storage: mechanism and optimization strategies toward commercialization. *Energ. Environ. Sci.* **2021,** *14* (4), 2244-2262.

45. Zhong, Y.; Shi, Q.; Zhu, C.; Zhang, Y.; Li, M.; Francisco, J. S.; Wang, H., Mechanistic Insights into Fast Charging and Discharging of the Sodium Metal Battery Anode: A Comparison with Lithium. *J. Am. Chem. Soc.* **2021,** *143* (34), 13929-13936.

46. Kamiyama, A.; Kubota, K.; Igarashi, D.; Youn, Y.; Tateyama, Y.; Ando, H.; Gotoh, K.; Komaba, S., MgO-Template Synthesis of Extremely High Capacity Hard Carbon for Na-Ion Battery. *Angew Chem Int Ed Engl* **2021,** *60* (10), 5114-5120.

47. Wang, H.; Yang, X.; Wu, Q.; Zhang, Q.; Chen, H.; Jing, H.; Wang, J.; Mi, S. B.; Rogach, A. L.; Niu, C., Encapsulating Silica/Antimony into Porous Electrospun Carbon Nanofibers with Robust Structure Stability for High-Efficiency Lithium Storage. *ACS Nano* **2018,** *12* (4), 3406-3416.

48. Chao, D.; Zhu, C.; Yang, P.; Xia, X.; Liu, J.; Wang, J.; Fan, X.; Savilov, S. V.; Lin, J.; Fan, H. J.; Shen, Z. X., Array of nanosheets render ultrafast and high-capacity Na-ion storage by tunable pseudocapacitance. *Nat Commun* **2016,** *7*, 12122.

49. Li, Q.; Liu, X.; Tao, Y.; Huang, J.; Zhang, J.; Yang, C.; Zhang, Y.; Zhang, S.; Jia, Y.; Lin, Q.; Xiang, Y.; Cheng, J.; Lv, W.; Kang, F.; Yang, Y.; Yang, Q. H., Sieving carbons promise practical anodes with extensible low-potential plateaus for sodium batteries. *Natl Sci Rev* **2022,** *9* (8), nwac084.

50. Liu, S.; Song, C.; Zhang, W.; Zhang, T.; Shao, W.; Weng, Z.; Yao, M.; Huang, H.; Jian, X.; Hu, F., Optimizing solvated anion accessibility and pseudocapacitive charge storage in carbon cathode toward high-energy sodium-ion capacitor. *Chem. Eng. J.* **2022,** *450*, 138103.

51. Zhang, L.; Wang, W.; Lu, S.; Xiang, Y., Carbon Anode Materials: A Detailed Comparison between Na- ion and K- ion Batteries. *Adv. Energy Mater.* **2021,** *11* (11).

52. Licht, S.; Douglas, A.; Ren, J.; Carter, R.; Lefler, M.; Pint, C. L., Carbon Nanotubes Produced from Ambient Carbon Dioxide for Environmentally Sustainable Lithium-Ion and Sodium-Ion Battery

Anodes. *ACS Central Science* **2016,** *2* (3), 162-168.
53. Sun, N.; Qiu, J.; Xu, B., Understanding of Sodium Storage Mechanism in Hard Carbons: Ongoing Development under Debate. *Adv. Energy Mater.* **2022,** *12* (27).